Journal of Science: Advanced Materials and Devices 10 (2025) 100893

Contents lists available at ScienceDirect

Journal of Science: Advanced Materials and Devices

journal homepage: www.elsevier.com/locate/jsamd

Research article

Shape anisotropy-induced local incoherent magnetization: Implications for magnetic sensor tuning

Jinwoo Kim [a], BB Nayak [a], I.V. Soldatov [b], R. Schäfer [b], Byeonghwa Lim [c,**], CheolGi Kim [a,*]

[a] Department of Physics and Chemistry, DGIST, Daegu, 42988, Republic of Korea
[b] Leibniz Institute for Solid State and Materials Research Dresden, Helmholtzstr. 20, D-01069, Dresden, Germany
[c] Department of Smartsensor Engineering, Andong National University, Andong, 36729, Republic of Korea

ARTICLE INFO

Keywords:
Magnetoresistive sensor
Planar Hall effect
Magnetization
Shape anisotropy
Demagnetizing field

ABSTRACT

The geometry of magnetoresistive sensors based on thin magnetic films plays a crucial role in shaping their magnetization behavior and overall performance. This study investigates Wheatstone bridge sensors made with NiFe single-layer films (thickness: 10–40 nm; width: 20–60 μm; length: 500 μm) to analyze the impact of shape anisotropy on magnetization distribution. We observed domain images and sensor signals by applying a magnetic field with a constant direction and strength while varying the strength of a second magnetic field applied perpendicularly to the first. Wide-field Kerr microscopy revealed that magnetization reversal occurs locally and incoherently, with the degree of incoherence increasing in geometries with stronger demagnetizing fields. The demagnetizing field in rectangular-shaped thin films was calculated, revealing a sharp increase in field strength 3–4 μm from the bridge element edge when magnetized in the short-length direction, which results in localized magnetization behavior. The sensor signals were calculated and measured for various width-to-length ratios of the bridge elements and external magnetic field strengths. Results show that variations in sensor geometry and external magnetic fields can influence peak-to-peak voltage by up to 41 % and make significant hysteresis in the sensor signal. These findings provide valuable insights into optimizing the design and performance of magnetoresistive sensors for advanced applications.

1. Introduction

In today's era of rapid technological advancement, the demand for sensors with enhanced sensitivity and reliability has grown significantly. Magnetic sensors, in particular, play a crucial role across various disciplines, including magnetic field detection, current sensing, biochips, automotive technology, drone technology, monitoring systems, and other applications [1–3]. The sensor detects variations in magnetic fields and converts them into corresponding electrical signals to precisely identify or record specific actions or conditions. Such a conversion can be based on the dependence of the resistance on the direction and strength of the applied magnetic field, a phenomenon known as magnetoresistance. Depending on the geometry and the stack of the sensor, one of the following effects can be observed: Anisotropic Magnetoresistance (AMR), Giant Magnetoresistance (GMR), and Tunnel Magnetoresistance (TMR) [4–8].

Magnetic sensors utilizing the AMR effect can employ two primary electrode configurations: (a) applied current and measured voltage parallel to each other and (b) both applied current and measured voltage are perpendicular to each other, which is known as Planar Hall Magnetoresistance (PHMR) [9,10]. PHMR sensor generally offers better resolution compared to GMR and TMR sensors due to its high linearity, thermal stability, simple structure that enables an easy fabrication process, and approximately 100 times lower 1/f noise [11–13]. Due to these advantages, PHMR sensors are gaining attention as a key candidate technology for precision magnetic field measurement and high-resolution sensor applications.

Various studies have been conducted to improve the performance of PHMR sensors, with a representative approach being the hysteresis reduction technique using ferromagnetic (FM)/antiferromagnetic (AFM) exchange bias systems [14–16]. Research has been conducted to enhance sensitivity by optimizing the exchange bias through

* Corresponding author. Daegu Gyeongbuk Institute of Science & Technology (DGIST), 333, Techno jungang-daero, Hyeonpung-eup, Dalseong-gun, Daegu, Republic of Korea.
** Corresponding author.
E-mail addresses: limbh@anu.ac.kr (B. Lim), cgkim@dgist.ac.kr (C. Kim).

https://doi.org/10.1016/j.jsamd.2025.100893
Received 4 March 2025; Received in revised form 16 April 2025; Accepted 20 April 2025
Available online 21 April 2025

adjustments to the thickness of the FM layer and the spacer at the FM/AFM interface. However, these studies have primarily focused on material-based approaches, and there is a lack of direct analysis of the impact of domain and magnetization distribution changes, which are the fundamental causes of sensor signal generation, on the signal itself.

In PHMR sensors, the signal is determined by the magnetization. In a sufficiently strong magnetic field, magnetization aligns itself in the direction of the magnetic field. In moderate fields, due to the specimen shape, thermal motion, or impurities and defects, the magnetization can locally deviate from the field direction [17–19]. Since the output signal of a PHMR sensor is formed by the superposition of individual domain signals in the active sensing region of the ferromagnetic layer, this incoherence might distort the sensor's output signal and impair its linearity, thus influencing the sensitivity. While these effects are often ignored when the sensor is sufficiently large, it is a critical factor that must be considered when aiming for miniaturization and performance enhancement [20–22].

No studies have directly observed and analyzed the impact of domain changes on the signal of PHMR sensors. Therefore, in this study, we designed a rectangular-shaped element in a Wheatstone bridge configuration to systematically analyze the effects of shape on the magnetic domain and magnetization distribution of ferromagnetic thin films. Rectangular-shaped elements induce a preferred magnetization along their length due to shape anisotropy. Different-sized rectangular-shaped elements were fabricated from a single-layer ferromagnetic thin film. The Wheatstone bridge structure, consisting of a single-layer ferromagnetic thin film, is particularly effective for studying the intrinsic magnetic properties of the ferromagnetic layer without the interference effects commonly found in multilayer structures. Based on this, the study aims to investigate the impact of shape anisotropy on the sensor's magnetization distribution and output signal, providing foundational data for the design and optimization of magnetoresistive sensors.

2. Material and methods

2.1. Materials and fabrication of magnetoresistive sensor

The sensor fabrication process employing DC magnetron sputtering commenced after the Si/SiO_2 (500 nm) substrate was cleaned using acetone, methanol, and deionized water. A Wheatstone bridge architecture was utilized, incorporating bridge elements with dimensions of width (20 μm–60 μm) × length (500 μm) and comprising a single-layer of NiFe with thicknesses of 10 nm–40 nm (Fig. 1). Patterning of the thin films was carried out via photolithography, utilizing AZ 5214 E photoresist in conjunction with AZ 300 MIF developer. During the DC magnetron sputtering deposition process, an external field of 400 Oe was applied via a magnetic holder to generate magnetization-induced anisotropy in the films. The deposition field was applied along the direction of the current-applying electrodes in the sensor, resulting in an induced anisotropy axis oriented at 45° with respect to the length of each bridge element. After the deposition, the photoresist was removed using acetone. After forming the sensor's layer, electrode patterns were delineated employing an identical lithographic procedure, followed by sputtering in the absence of an applied field. The electrode thin films comprised a bilayer of Ta (5 nm)/Au (100 nm).

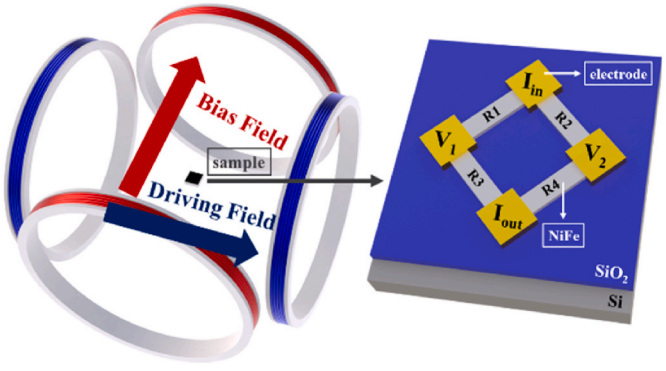

Fig. 1. Schematics of external field configuration with Wheatstone bridge sensor.

2.2. Magnetic domain observation and characterization of magnetoresistive sensor

The sensor was placed at the center of a two-axis coil system, where two mutually perpendicular magnetic fields were applied during the measurement. The driving field, aligned parallel to the voltage-sensing electrodes, was swept in strength during the measurement. The bias field, oriented parallel to the current-applying electrodes, was maintained at a constant strength throughout the measurement. The strengths of both magnetic fields were controlled by adjusting the current supplied to each coil, with a constant current source used for the bias field coil to ensure field stability. Magnetic domain images in both longitudinal (vertical within the image plane) and transverse (horizontal within the image plane) sensitivity directions were acquired simultaneously using a wide-field magneto-optical Kerr effect (MOKE) microscope with polarized light (457 nm) [23]. The local magnetization angle of the sensor bridge was derived using quantitative Kerr microscopy based on the combination of images with complementary, orthogonal in-plane sensitivity axes and a contrast calibration that was performed in advance by measuring sensitivity functions in a rotating in-plane magnetic saturation field [24]. The sensor characteristics were determined by applying a constant current to the sensor and measuring the output voltage transverse to the current direction. The signals were recorded using a conventional transport measurement setup, which includes a Keithley 2400 sourcemeter and a Keithley 34401 A multimeter, interfaced with LabVIEW software.

3. Results and discussion

3.1. Local incoherent magnetization in Wheatstone bridge sensor

The local incoherent magnetization of a sensor bridge with a film thickness of 40 nm, element width of 40 μm, and length of 500 μm was analyzed using a Kerr microscope. The external field was swept in the horizontal direction (driving field), while the additional constant bias field of 10 Oe was applied along the vertical direction. Upon the sweep in a positive direction (Fig. 2(a)), when the driving field of −20 Oe was applied (total field of 22 Oe at 153°), the single magnetic domain in all bridge elements was observed, implying the magnetization to be coherent within the whole element area as shown for R1 and R2 bridge elements in Fig. 2(a) (1) and (1'). When the driving field changed to −10 Oe (total field of 135° at 14 Oe), the R2 bridge element maintained a single-domain state in Fig. 2(a) (2′), whereas the R1 bridge element in Fig. 2(a) (2) exhibited incoherent magnetization in which the central domain rotated first and then separate domains were formed at both edges with delayed rotation. When the driving field was 0 Oe (total field of 90° at 10 Oe), the magnetization of the R1 bridge element in Fig. 2(a) (3) was generally aligned along the longitudinal direction of the bridge, but irregular domain wall modulation was observed at the edges. In contrast, the magnetization of the R2 bridge element in Fig. 2(a) (3′) maintained an overall coherent state (Fig. S1). As shown in Fig. 2(a) (4) and (4′), when the driving field changes to +10 Oe (total field of 14 Oe at 45°), the magnetization of the R1 bridge element rotates coherently, whereas in the R2 bridge element, new magnetic domains are formed at the periphery, causing incoherent magnetization, and the generated magnetic domains also show a rotational delay phenomenon. Finally, when the driving field is further increased to +20 Oe (total field of 22 Oe at 27°), both bridge elements show coherent magnetization states again in Fig. 2(a) (5) and (5′).

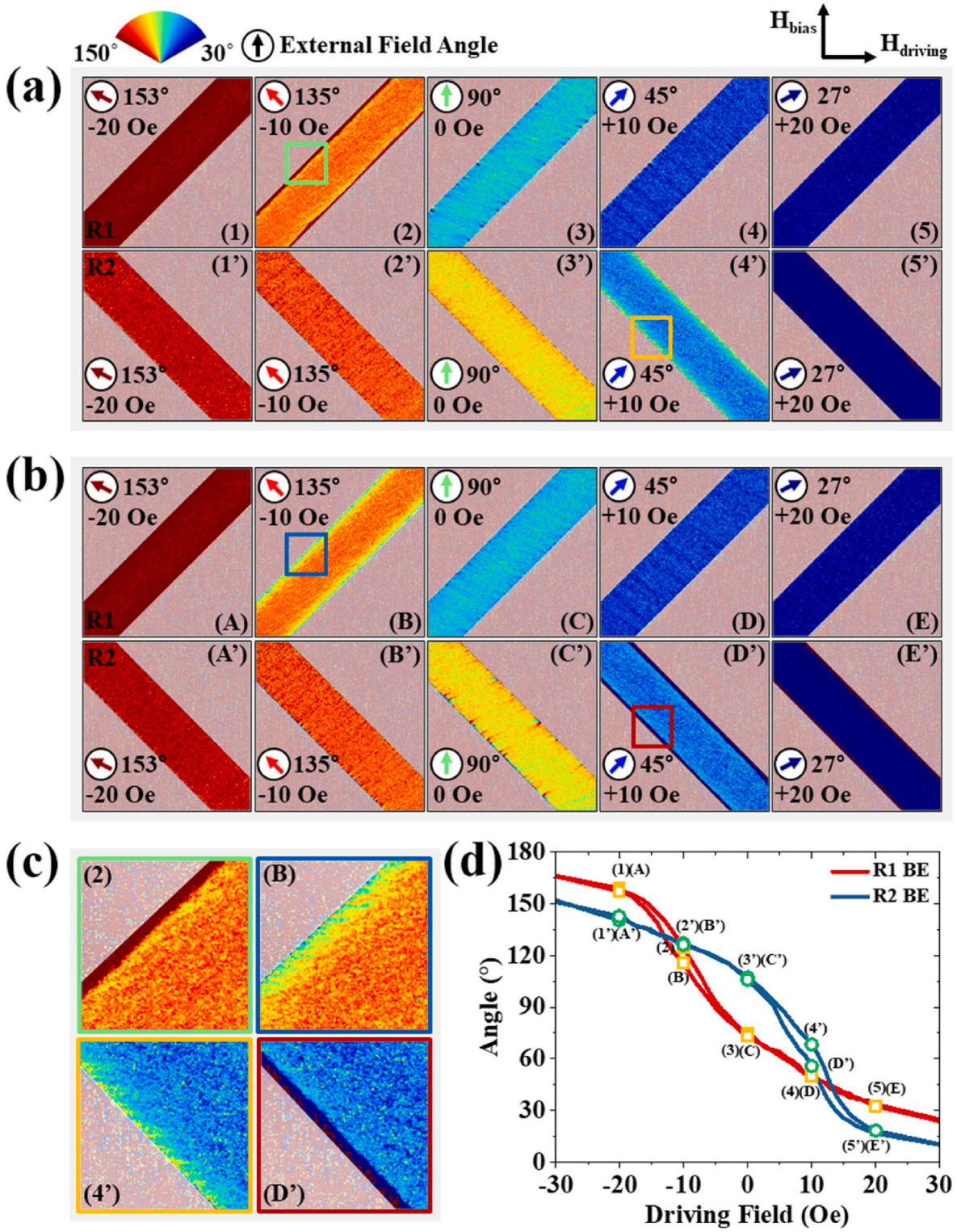

Fig. 2. The magnetic domain images in different driving fields applied to the bridge elements (BE): thickness 40 nm, width 40 μm, length 500 μm, and with a constant 10 Oe bias field. (a) The domains were observed during increasing and (b) decreasing driving fields. The angle and strength of the driving field are indicated in each image. (c) Zoom-in magnetic domain images at the edges show local incoherent magnetization according to the direction of driving field change. (d) The average magnetization angle across the element area as a function of the driving field.

When the driving field was swept in reversed direction (from positive to negative field), the corresponding magnetic domains were recorded, as shown in Fig. 2(b). In the driving field of −10 Oe within the R1 bridge element and driving field +10 Oe within the R2 bridge element, the local magnetization angles at the outer edges differ from those in the element center, and opposite to that in Fig. 2(a). So, when the direction of the driving field sweep is reversed, the magnetization angle at the center of the bridge follows the field and points in the same direction as for the initial sweep (Fig. 2(a)), while the magnetization at the edge lags in opposite as can be seen from Fig. 2(c). In the driving field of 0 Oe,

irregular domain wall modulation was observed in the R2 bridge element in Fig. 2(b)(C′) during the field sweep from positive to negative, unlike the case of the sweep from negative to positive with Fig. S1. This indicates the difference that arises depending on whether the external field is swept from the width to the length of the element or from the length to the width of the element.

From these results, it can be observed that the incoherent magnetization regions typically occur at the edges. The changes in the domain can be classified into two cases: when the field sweeps from the width direction to the length direction and when the field sweeps from the length direction to the width direction. The difference between these two cases can be seen in the enlarged rectangular area (highlighted in Fig. 2(a) and (b)) shown in Fig. 2(c)). When the field sweeps from the width direction to the length direction, the domain at the edges separates from the center and aligns with the previous magnetization before splitting into smaller regions and transitioning to a homogeneous magnetization. In contrast, when the field sweeps from the length direction to the width direction, a homogeneous magnetization is maintained, but new smaller domains are formed at the boundaries, with delayed rotation, eventually leading to a coherent magnetization. This rotational delay effect induces a hysteresis effect, as seen in the average magnetization angle of each bridge element in Fig. 2(d). Therefore, when applied to the same external field, the magnetization angle in one case remains uniform across the structure, while in another case, hysteresis caused by rotation delay at the edges is observed.

The magnetization of the bridge elements was observed for various widths under different bias fields (Fig. 3 and Fig. S2–S3). In the case of the R1 bridge element, when the field sweeps from the width direction to the length direction, the edge domains with rotational delay at 135° split into smaller domains when they reach 90° and then transition into a uniform domain in the bridge elements with widths of 40 μm and 60 μm. However, in the width 20 μm, the domain splitting, initially confined to the edges, extends across the entire width of the bridge element before transitioning into a uniform domain. On the other hand, when the thickness 20 nm, or bias field strength increases to 25 Oe and 50 Oe, the bridge elements exhibit coherent magnetization regardless of the field change.

Under the condition where the driving field increases from the negative to the positive direction when the external magnetic field is applied along the width direction of the R1 bridge element, the domain angle remains relatively constant near the center but exhibits a sharp change at a specific area near the edges. As shown in Fig. S4(a), abrupt changes occur within approximately 5 μm from the lateral sides of the rectangular element. These regions are defined as the domain edges of the rectangular structure. In the case of the R2 bridge element, when the external magnetic field is applied along the width direction, the domain angle also increases toward the edges, but unlike R1 bridge element, it changes in a relatively gradual parabolic manner (Fig. S4(b)). Notably, under a bias field of 10 Oe, no distinct boundary of the incoherent region was observed. The proportion of the incoherent region relative to the entire bridge element was calculated under various width and bias field conditions, and it was found to decrease as the width and bias field strength increased (Fig. S4(c–d)). In conclusion, incoherent regions are more prominent when the bridge element has a smaller width and is subjected to a weaker bias field.

The magnetization reversal curve can be derived by plotting the normalized values of the average element image intensity, similar to that typically obtained by magnetometry (M − H loops). Magnetization curves, derived from Kerr data during field sweeps, are shown in Fig. 4 and were obtained for various bias fields and film widths. As the bias field strength increases, stronger driving fields are required to align the magnetization in the driving field's direction. The magnetization curves of the R1 and R2 bridge elements exhibit asymmetry with respect to the M/M_S axis under the applied field while simultaneously showing rotationally symmetric responses to each other. Additionally, all magnetization curves demonstrate an offset when the driving field was zero. Compared to Fig. S5, these characteristics become more pronounced in thin films with narrower widths or greater thicknesses, and the asymmetry decreases when a strong bias field is applied.

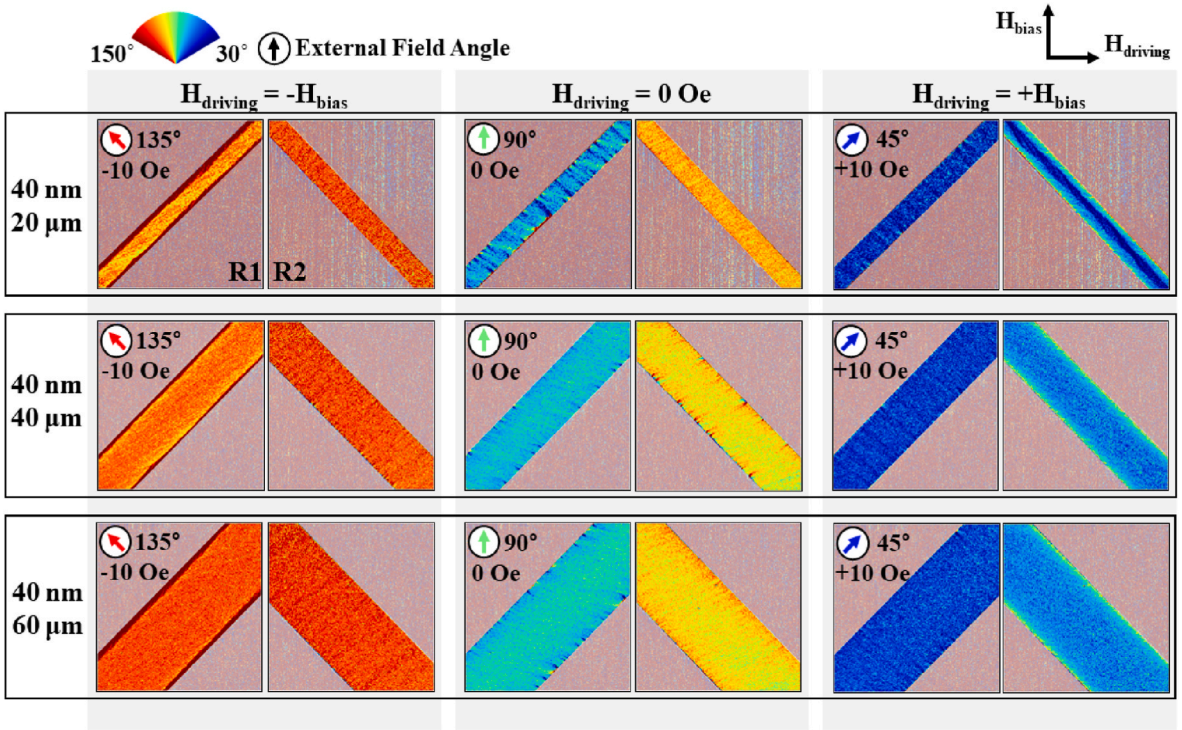

Fig. 3. The magnetic domain images within the bridge elements: thickness 40 nm, width 20 μm–60 μm, and length 500 μm for different driving fields with a constant 10 Oe bias field.

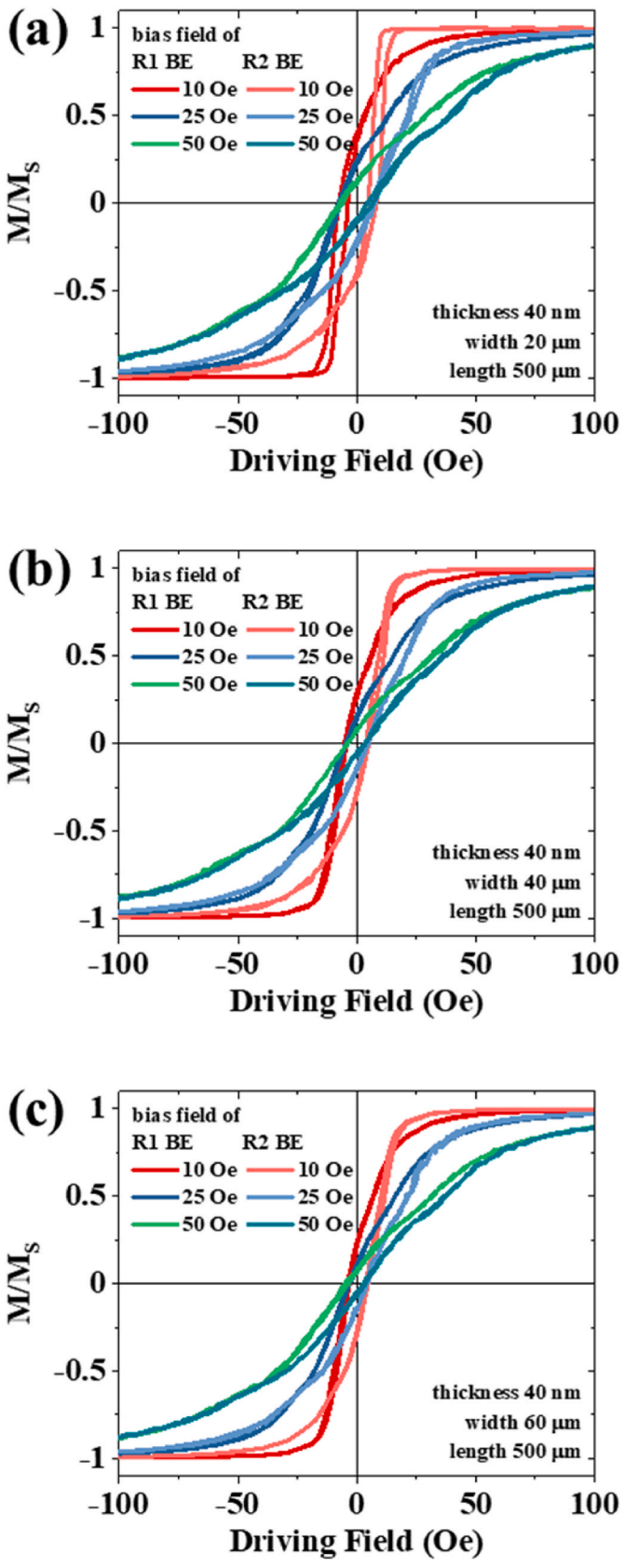

Fig. 4. Magnetization curve of the R1 and R2 bridge elements (BE). Bridges with a thickness 40 nm, length 500 μm and width (a) 20 μm, (b) 40 μm, and (c) 60 μm for different bias fields. Different magnetization curves are revealed for the R1 and R2 bridges during the cycling of the driving field.

3.2. Demagnetizing field across shape anisotropy

The shape of a magnetic specimen influences its magnetic characteristics, a phenomenon known as shape anisotropy. Shape anisotropy arises from variations in the demagnetizing field caused by the geometry of the magnetic material. It is described by demagnetizing field H_d, an internal field in the direction opposite to the magnetization written as [25]:

$$H_d = -NM \quad \text{(Eq.1)}$$

where N is demagnetization factor, and M is magnetization, calculated as the average of the magnetization distribution across the entire bridge element. Since the value of N varies depending on the shape and direction, the internal field of the magnetic specimen also changes with direction, which becomes a key factor in determining the preferred direction of magnetization.

Shape anisotropy significantly influences the hysteresis and asymmetry characteristics of the magnetization. To understand shape anisotropy, if the magnetization M is assumed to be the average value of the overall magnetization distribution of the bridge element and the shape factor N is considered a constant, a uniform demagnetizing field is formed within the magnetic material, opposing the average magnetization. This approach is not a significant issue in bulk magnetic materials because the demagnetizing field strength is weak due to the small value of N. However, N and M cannot be assumed constant in microscale thin-film patterns such as PHMR sensors. This is because, even if M remains uniform throughout the magnetic material, the demagnetizing field H_d can vary significantly depending on the position.

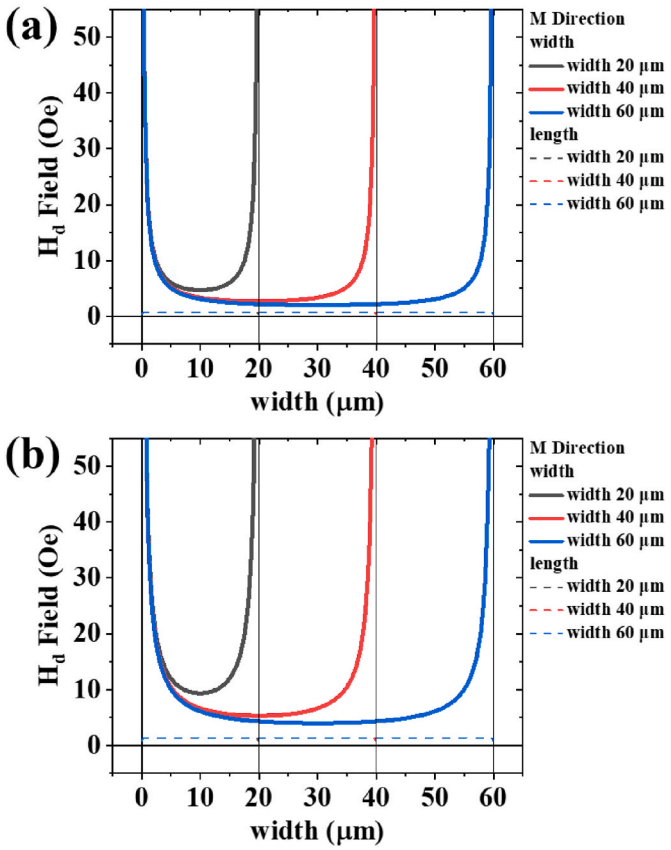

Fig. 5. The simulated demagnetizing field of a bridge element with a thickness (a) 20 nm and (b) 40 nm. The solid line represents the state of saturation along the width direction of the bridge element, while the dashed line represents saturation along the length direction. The field strength increases sharply from the center to the element's edges.

Fig. 5 presents the calculated strength of the demagnetizing field when the bridge element is magnetized to saturation along the width and length. According to the simulation results, the demagnetizing field is weakest at the element's center and increases sharply toward the edges. Notably, the minimum value of the demagnetizing field at the center tends to increase as the width decreases, whereas, in the outer regions, the demagnetizing field remains nearly constant regardless of the width.

Since the demagnetizing field acts opposite the magnetization, a field stronger than the demagnetizing field is required to align the magnetization with the external field. In the experiment, magnetization alignment became difficult when a total field of 14 Oe was applied in the width direction (45° or 135°) in regions where the demagnetizing field exceeded this value. Consequently, as Figs. 2 and 3 observed, domains exhibiting rotational lag appeared in the outer regions where the demagnetizing field was stronger than the total field.

In particular, for a thickness of 40 nm, the region where the demagnetizing field exceeded the total field developed more rapidly when the element was magnetized along the width direction. Specifically, for a thickness of 20 nm, the demagnetizing field exceeded 14 Oe within approximately 1.6 μm from the edges, whereas for a thickness of 40 nm, this occurred within a 3–4 μm range. This suggests that the demagnetizing field distribution changes as the thickness increases, making magnetization alignment more difficult in the outer regions.

When bias fields of 25 Oe or 50 Oe were applied, the total field along the width or length direction of the bridge elements became 35 Oe or 71 Oe, respectively. In these cases, the regions where the total field exceeded the calculated demagnetizing field were broader compared to the case of a 10 Oe bias field, leading to a wider uniform magnetization region at the center of the element. However, since the demagnetizing field in the outer regions remained larger than the total field applied, local magnetization effects still appeared at the edges.

When the external field was applied along the length direction of each bridge element, the simulated longitudinal demagnetizing field was significantly lower than the transverse demagnetizing field observed when the magnetization was aligned along the width direction (Fig. S6). In contrast to the width-aligned case, the strength of the longitudinal demagnetizing field increased with the bridge width, and it was higher for the 40 nm thick films than for the 20 nm ones. In all cases, the external field was strong enough to magnetize the bridge element along the length direction. The simulation results effectively explain the observed domain images.

3.3. Analysis of magnetoresistive sensor characteristics with Wheatstone bridge

Using the known equations of the magnetoresistance effect, the magnetoresistance can be calculated based on the magnetic material's current and magnetization. However, as observed in the experimental results of this study, when the magnetization of the magnetic material is not uniform across all regions, assuming a constant magnetization for calculations is not appropriate. This is because the actual magnetization distribution varies depending on the position, meaning an averaged magnetization value cannot accurately reflect the experimental results. Therefore, an approach that considers the local magnetization distribution is required.

In terms of resistivities, $\rho_{\perp}$ and $\rho_{\parallel}$ represent the resistivity at saturation field, transverse and longitudinal to the current direction, respectively, with $\Delta\rho$ being $\rho_{\perp} - \rho_{\parallel}$. The resistance R_{rect} of a rectangular object made of ferromagnetic material is denoted as [26]:

$$R_{\mathrm{rect}} = \frac{l}{wt}\left(\rho_{\perp} + \Delta\rho\left(cos^2\,\theta\,cos^2\,\gamma + sin^2\,\theta\,sin^2\,\gamma\right) + \frac{\Delta\rho}{2}sin\,2\theta\,sin\,2\,\gamma\right) \quad \text{(Eq.2)}$$

where θ and γ are the magnetization angle and the current angle with respect to the direction of the applied driving field. Wheatstone bridge is a circuit consisting of four resistors, and the resistance of each bridge R_{bridge} is

$$R_1 = R_4 = \frac{l}{wt}\left(\rho_{\perp} + \frac{\Delta\rho}{2}(1 + \sin(2\theta))\right) \quad \text{(Eq.3)}$$

$$R_2 = R_3 = \frac{l}{wt}\left(\rho_{\perp} + \frac{\Delta\rho}{2}(1 - \sin(2\theta))\right) \quad \text{(Eq.4)}$$

This equation assumes that opposite bridge elements have the same resistivity. However, in the case of anisotropic magnetoresistance materials, which do not ensure a coherent magnetization throughout each element, the resistivity may not be uniform across all areas of the object. When the area of the bridge element is divided into n × m regions, the width of the cell is w/m, and the length of the cell is l/n. The resistance of any single cell in a Wheatstone bridge sensor should be addressed independently as

$$R_{\mathrm{cell}} = \frac{m}{n}\frac{l}{wt}\left(\rho_{\perp} + \frac{\Delta\rho}{2}(1 \pm \sin(2\theta))\right) \quad \text{(Eq.5)}$$

where i and j represent the indices of the cells. Consequently, the sum of the resistances of all cells yields the output signal of one bridge element.

$$R_{\mathrm{length}} = \left[\sum_{i=1}^{n} R_{\mathrm{cell(i,1)}}, \sum_{i=1}^{n} R_{\mathrm{cell(i,2)}}, \cdots, \sum_{i=1}^{n} R_{\mathrm{cell(i,m)}}\right] \quad \text{(Eq.6)}$$

$$R_{\mathrm{bridge}} = \left(\sum_{j=1}^{m} \left(R_{\mathrm{length\ (j)}}\right)^{-1}\right)^{-1} \quad \text{(Eq.7)}$$

where R_{length} is the sum of the resistances arranged in the specific column in divided regions. The output voltage of the Wheatstone bridge V_{total} is given by the potential difference between nodes V_1 and V_2, and can therefore be expressed as follows:

$$\mathrm{V_{total}} = \frac{\mathrm{I}}{2}(R_1 - R_2) \quad \text{(Eq.8)}$$

where I represents the current supplied to the Wheatstone bridge.

Fig. 6 shows the results of two different methods for calculating the output voltage in the Wheatstone bridge sensor. The normalization of the calculated signal was performed using the greater of the two absolute peak voltages obtained under a bias field of 50 Oe. Accordingly, the normalized voltage was defined as:

$$\frac{V}{\left|V_{peak}\ (bias\ field)\right|}, \text{where } \left|V_{peak}\ (bias\ field)\right| = max(|V_{max}|, |V_{min}|) \quad \text{(Eq.9)}$$

The whole signal is the sum of the signals from each bridge element. For the R1&R4 bridge elements, a positive offset is observed, while for the R2&R3 bridge elements, a negative offset is observed. The total output voltage of the sensor, which was calculated, and the R1 and R4 bridge elements are symmetric about the origin of the R2 and R3 bridge elements. The sum of the signals from four bridge elements, and the signal is close to linear and passes zero in zero field due to offset compensation based on the symmetry relationship between the bridge elements.

Fig. 6(a) shows the output voltage calculated for a single bridge element based on the average magnetization angle distribution, assuming uniform magnetization rotation. This calculation follows Eq. (3) and Eq. (4). In contrast, Fig. 6(b) presents the sensor's output voltage estimated using Eq. (7), which accounts for the non-uniform distribution of the measured magnetization angles.

The output voltage calculated considering the non-uniform distribution consistently exhibited a lower peak-to-peak voltage than the one based on the average magnetization angle distribution. This indicates that even if the net magnetization direction remains the same, differences in sensor output signals can arise between coherent and

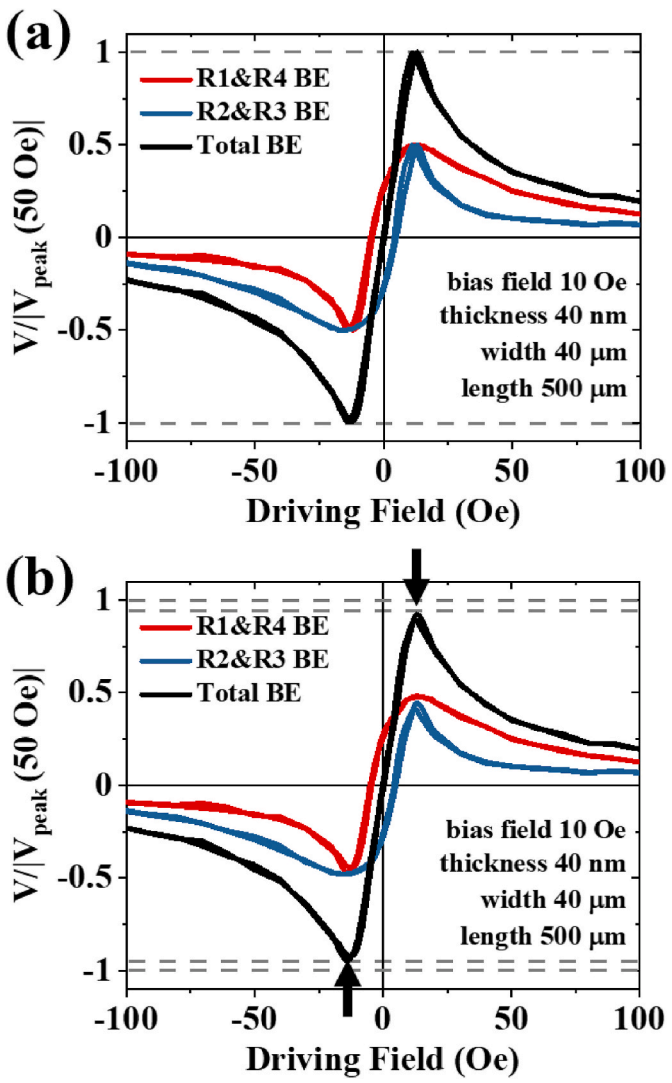

Fig. 6. The magnetoresistive sensor signal is calculated for each bridge using (a) a coherent magnetization angle and (b) an incoherent magnetization angle. Different sensor signals are revealed for the R1 and R2 bridge elements (BE) during a cyclic driving field.

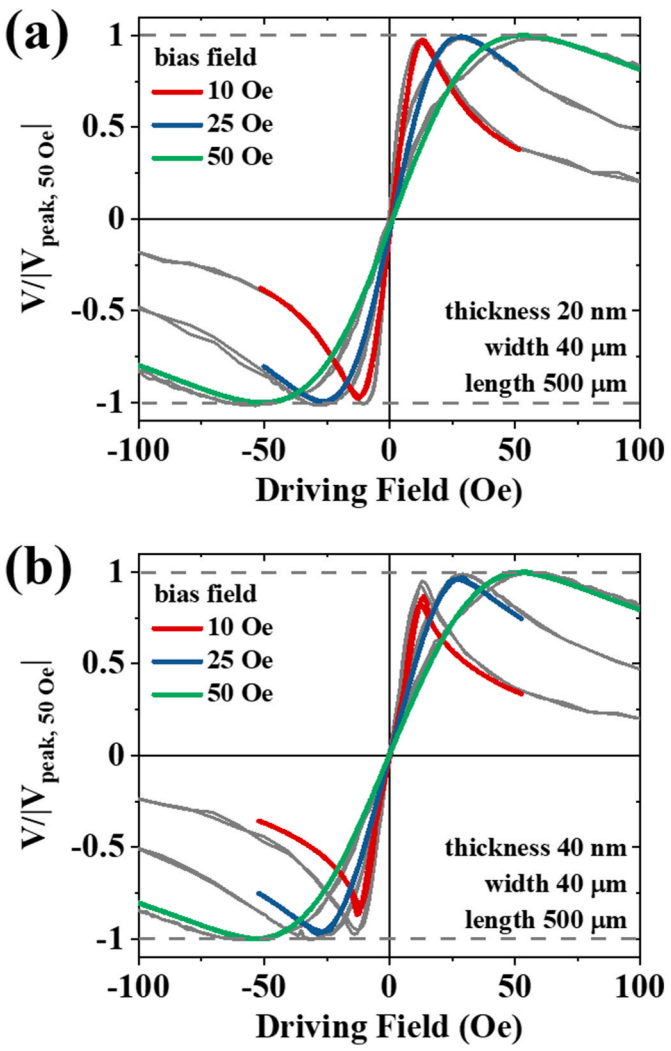

Fig. 7. Measured and calculated planar Hall voltage signals on the sensor's driving field. Bridges with (a) thickness 20 nm width 40 μm and (b) thickness 40 nm, width 40 μm for different bias fields. The black solid line represents the calculated sensor signal depending on the observed magnetic domain.

incoherent magnetization cases. Furthermore, it suggests that variations in magnetization non-uniformity can lead to differences in the sensor's output signal.

The calculated results were compared with the actual sensor signals. As shown in Fig. 7 and Fig. S7, the sensor signals were computed using Eq .(7) based on domain images and then compared with the measured signals. The sensor signals varied depending on the strength of the bias field and the shape of the thin film, with some curves exhibiting hysteresis. Signal calculations were performed for thin films with thicknesses of 20 nm and 40 nm. The results showed that for the 20 nm thick film, the calculated and measured signals matched closely. In contrast, for the 40 nm thick film, the discrepancy between the two signals increased as the bias field decreased.

Additionally, a decrease in peak-to-peak voltage was observed as the bias field strength decreased (Fig. S8), with the peak-to-peak voltage decreasing by up to 41 %, depending on the sensor size and bias field strength. This discrepancy is attributed and the possibility that, as the film thickness increases and the applied field weakens, the internal magnetization differs from the surface magnetization or exhibits a more complex distribution. This interpretation aligns with the hysteresis analysis of the sensor in response to changes in thickness and driving field direction (Table S1), where thinner films and wider lines showed minimal differences between sensor signals, which effectively supports the previous findings.

4. Conclusion

This study investigated the effects of sensor shape and bias field on magnetization distribution and sensor signals. Using Kerr effect microscopy, magnetic domain analysis revealed that rotational lag occurs at the sensor boundaries due to the demagnetizing field, forming multi-domains. These domain structures were identified as key factors determining the sensor characteristics. The sensor signal exhibited a decreasing trend with increasing film thickness and decreasing width while asymmetry and hysteresis increased. Notably, the sensor output voltage was lower in a multi-domain state than in a single-domain state, even when the net magnetization points in the same direction. Additionally, the bias field significantly influenced sensor characteristics, with stronger bias fields reducing asymmetry and hysteresis. The bias field cannot produce the same results as the exchange bias field; however, this result implies that exchange bias is a crucial factor in the sensor design and fabrication process. This study precisely analyzes shape anisotropy and local incoherent magnetization, contributing to a deeper understanding of sensor operation principles. These findings are

expected to serve as fundamental data for the practical advancement of magnetic sensor technology.

CRediT authorship contribution statement

Jinwoo Kim: Writing – review & editing, Writing – original draft, Investigation, Formal analysis, Data curation, Conceptualization. **BB Nayak:** Writing – review & editing. **I.V. Soldatov:** Writing – review & editing, Formal analysis, Data curation. **R. Schäfer:** Writing – review & editing. **Byeonghwa Lim:** Writing – review & editing, Writing – original draft, Investigation, Formal analysis, Conceptualization. **CheolGi Kim:** Writing – review & editing, Supervision, Resources, Conceptualization.

Declaration of competing interest

The authors declare that they have no known competing financial interests or personal relationships that could have appeared to influence the work reported in this paper.

Acknowledgments

The authors acknowledge funding from the National Research Foundation of Korea (NRF) grant funded by the Korean government (MSIT) (Grant No. NRF-2018R1A5A1025511) and in part by the R&D program of MOTIE (Grant No. 00236809).

Appendix A. Supplementary data

Supplementary data to this article can be found online at https://doi.org/10.1016/j.jsamd.2025.100893.

References

[1] L. Jogschies, D. Klaas, R. Kruppe, J. Rittinger, P. Taptimthong, A. Wienecke, L. Rissing, M. Wurz, Recent developments of magnetoresistive sensors for industrial applications, Sensors 15 (2015) 28665–28689, https://doi.org/10.3390/s151128665.

[2] A.D. Henriksen, G. Rizzi, F.W. Østerberg, M.F. Hansen, Optimization of magnetoresistive sensor current for on-chip magnetic bead detection using the sensor self-field, J. Magn. Magn Mater. 380 (2015) 209–214, https://doi.org/10.1016/j.jmmm.2014.09.056.

[3] V.C. Martins, F.A. Cardoso, J. Germano, S. Cardoso, L. Sousa, M. Piedade, P. P. Freitas, L.P. Fonseca, Femtomolar limit of detection with a magnetoresistive biochip, Biosens. Bioelectron. 24 (2009) 2690–2695, https://doi.org/10.1016/j.bios.2009.01.040.

[4] E.M. Pugh, Hall effect and the magnetic properties of some ferromagnetic materials, Phys. Rev. 36 (1930) 1503–1511, https://doi.org/10.1103/PhysRev.36.1503.

[5] M.N. Baibich, J.M. Broto, A. Fert, F.N. Van Dau, F. Petroff, P. Etienne, G. Creuzet, A. Friederich, J. Chazelas, Giant magnetoresistance of (001)Fe/(001)Cr magnetic superlattices, Phys. Rev. Lett. 61 (1988) 2472–2475, https://doi.org/10.1103/PhysRevLett.61.2472.

[6] G. Binasch, P. Grünberg, F. Saurenbach, W. Zinn, Enhanced magnetoresistance in layered magnetic structures with antiferromagnetic interlayer exchange, Phys. Rev. B 39 (1989) 4828–4830, https://doi.org/10.1103/PhysRevB.39.4828.

[7] M. Julliere, Tunneling between ferromagnetic films, Phys. Lett. 54 (1975) 225–226, https://doi.org/10.1016/0375-9601(75)90174-7.

[8] T. Miyazaki, N. Tezuka, Giant magnetic tunneling effect in Fe/AlzO3/Fejunction, J. Magn. Magn Mater. (1995).

[9] C. Goldberg, R.E. Davis, New galvanomagnetic effect, Phys. Rev. 94 (1954) 1121–1125, https://doi.org/10.1103/PhysRev.94.1121.

[10] V.D. Ky, Planar Hall effect in ferromagnetic films, Phys. Status Solidi 26 (1968) 565–569, https://doi.org/10.1002/pssb.19680260220.

[11] T. Jeon, J.H. Lee, A. Talantsev, C.G. Kim, Planar Hall resistance sensor with improved thermal stability, IEEE Magn. Lett. 10 (2019) 1–5, https://doi.org/10.1109/LMAG.2019.2943054.

[12] J. Lee, C. Jeon, T. Jeon, P. Das, Y. Lee, B. Lim, C. Kim, Bridge resistance compensation for noise reduction in a self-balanced PHMR sensor, Sensors 21 (2021) 3585, https://doi.org/10.3390/s21113585.

[13] M. Mahfoud, Q.-H. Tran, S. Wane, D.-T. Ngo, E.H. Belarbi, A. Boukra, M. Kim, A. Elzwawy, C. Kim, G. Reiss, B. Dieny, A. Bousseksou, F. Terki, Reduced thermal dependence of the sensitivity of a planar Hall sensor, Appl. Phys. Lett. 115 (2019) 072402, https://doi.org/10.1063/1.5110671.

[14] A. Elzwawy, S. Kim, A. Talantsev, C. Kim, Equisensitive adjustment of planar Hall effect sensor's operating field range by material and thickness variation of active layers, J. Phys. D Appl. Phys. 52 (2019) 285001, https://doi.org/10.1088/1361-6463/ab18f2.

[15] T.Q. Hung, S. Oh, B. Sinha, J.-R. Jeong, D.-Y. Kim, C. Kim, High field-sensitivity planar Hall sensor based on NiFe/Cu/IrMn trilayer structure, J. Appl. Phys. 107 (2010) 09E715, https://doi.org/10.1063/1.3337739.

[16] D.T. Bui, M.D. Tran, H.D. Nguyen, H.B. Nguyen, High-sensitivity planar Hall sensor based on simple gaint magneto resistance NiFe/Cu/NiFe structure for biochip application, Adv. Nat. Sci. Nanosci. Nanotechnol. 4 (2013) 015017, https://doi.org/10.1088/2043-6262/4/1/015017.

[17] H. Kikuchi, S. Kamata, T. Nakai, S. Hashi, K. Ishiyama, Influence of demagnetizing field on thin-film GMI magnetic sensor elements with uniaxial magnetic anisotropy, Sensor Actuator Phys. 230 (2015) 142–149, https://doi.org/10.1016/j.sna.2015.04.027.

[18] J. Liu, A. Singh, J. Llandro, L.B. Duffy, M.R. Stanton, S.N. Holmes, M.J. Applegate, R.T. Phillips, T. Hesjedal, C.H.W. Barnes, A low-temperature Kerr effect microscope for the simultaneous magneto-optic and magneto-transport study of magnetic topological insulators, Meas. Sci. Technol. 30 (2019) 125201, https://doi.org/10.1088/1361-6501/ab39b4.

[19] K. Xu, D.K. Schreiber, Y. Li, B.R. Johnson, J. McCloy, Effect of defects, magnetocrystalline anisotropy, and shape anisotropy on magnetic structure of iron thin films by magnetic force microscopy, AIP Adv. 7 (2017) 056806, https://doi.org/10.1063/1.4976580.

[20] V. Mor, M. Schultz, O. Sinwani, A. Grosz, E. Paperno, L. Klein, Planar Hall effect sensors with shape-induced effective single domain behavior, J. Appl. Phys. 111 (2012) 07E519, https://doi.org/10.1063/1.3680084.

[21] A.D. Henriksen, G. Rizzi, M.F. Hansen, Experimental comparison of ring and diamond shaped planar Hall effect bridge magnetic field sensors, J. Appl. Phys. 118 (2015) 103901, https://doi.org/10.1063/1.4930068.

[22] Y.S. Huang, C.C. Wang, A.O. Adeyeye, D. Tripathy, Planar Hall effect in orthogonal submicrometer Co wires, J. Appl. Phys. 99 (2006) 08C508, https://doi.org/10.1063/1.2165131.

[23] I. Soldatov, R. Schäfer, Selective sensitivity in Kerr microscopy, Rev. Sci. Instrum. 88 (2017) 073701, https://doi.org/10.1063/1.4991820.

[24] I.V. Soldatov, R. Schäfer, Advances in quantitative Kerr microscopy, Phys. Rev. B 95 (2017) 014426, https://doi.org/10.1103/PhysRevB.95.014426.

[25] B.D. Cullity, C.D. Graham, Introduction to Magnetic Materials, second ed., IEEE/Wiley, Hoboken, N.J, 2009.

[26] B. Lim, M. Mahfoud, P.T. Das, T. Jeon, C. Jeon, M. Kim, T.-K. Nguyen, Q.-H. Tran, F. Terki, C. Kim, Advances and key technologies in magnetoresistive sensors with high thermal stabilities and low field detectivities, APL Mater. 10 (2022) 051108, https://doi.org/10.1063/5.0087311.